Proceedings of the Eighteenth International Conference on
Civil, Structural and Environmental Engineering Computing
Edited by: P. Iványi, J. Kruis and B.H.V. Topping
Civil-Comp Conferences, Volume 10, Paper 3.5
Civil-Comp Press, Edinburgh, United Kingdom, 2025
ISSN: 2753-3239, doi: 10.4203/ccc.10.3.5

Experimental and Numerical Investigation on the Mechanical Behavior of 3D Star-Shaped Auxetic Structure

L. Meng[1], Y. Hou[2] and W. Han[2]

[1]State IJR Center of Aerospace Design and Additive Manufacturing, Northwestern Polytechnical University, Xi'an, China
[2]School of Mechanical and Power Engineering, Zhengzhou University, China

Abstract

This study proposes a novel 3D star-shaped auxetic (3D-SAU) structure, and further investigates the mechanical behavior using experimental and numerical approaches. Three lattice structures have been initially designed and additively-manufactured, namely 3D-SAU, as well as the conventional body-centered-cubic (BCC) and 3D re-entrant (3D-RE) structures. Quasi-static compressive and low-velocity impact (LVI) tests have been performed on those additively-manufactured structures, to characterize the mechanical properties. The experimental and numerical results indicate that 3D-SAU structure possesses a more stable and prolonged stress plateau stage than BCC and 3D-RE structures, demonstrating its superior protective capacity. Moreover, LVI test results reveal that the structures with auxetic effect exhibit lower peak forces and longer impact durations compared to BCC structure. Both auxetic structures are found to possess better energy-absorption capacity during high energy impact cases.

Keywords: 3D auxetic structure, mechanical properties, quasi-static compression, low-velocity impact, energy absorption, additive manufacturing.

1 Introduction

Mechanical metamaterials are artificially engineered materials with exceptional physical properties that are rarely observed in nature[1]. Auxetic metamaterials, a subset of mechanical metamaterials, exhibit the negative Poisson's ratio (NPR) effect, where they expand or shrink laterally when stretched or compressed. Due to their

unique deformation mechanisms, auxetic metamaterials offer advantages over traditional materials, including high toughness, shear resistance, energy absorption, and indentation resistance[2-4]. These properties make auxetic metamaterials ideal application in industries such as aerospace, automotive, and sports[5,6].

Most existing studies on auxetic metamaterials have focused on the design of 2D auxetic cells, while 3D auxetic ones have been studied less extensively[7,8]. However, 2D auxetic metamaterials are limited by high mass density, inflexible configurations, and confinement to a single plane, which significantly restrict their practical applications[9]. Hence, developing novel 3D auxetic structures is essential to expanding the application range of auxetic metamaterials.

To further explore the potential of auxetic metamaterials in impact resistance and energy absorption, this paper proposes a novel 3D star-shaped auxetic (3D-SAU) structure. The body-centered-cubic (BCC) and 3D re-entrant (3D-RE) structures, known for their excellent specific stiffness and auxetic characteristics, are selected as reference structures for comparison. The mechanical properties of the 3D-SAU structure are evaluated both experimentally and numerically through quasi-static compression and low-velocity impact (LVI) tests. The 3D-SAU structure is designed to exhibit a prolonged low-stress plateau and enhanced energy absorption efficiency. Detailed methods and results are presented in the following sections.

2 Lattice structures

2.1 Design strategy of 3D-SAU

Fig. 1 illustrates the conceptual design of the 3D-SAU structure, which is composed of two layers of star-shaped frames, and these frames are interconnected by supporting rods. The unit cell of the 3D-SAU structure is presented in Fig. 1b, to illustrate the connection approach between different frames. It consists of two star-shaped frames connected by six supporting rods, and each frame possesses three concave points and three convex points. Due to the staggered alignment, the concave points of the upper frame are connected with the convex points of the bottom frame.

In addition, the structural parameters of the unit cell are presented in Figs. 1c and d. As shown in Fig. 1c, each star-shaped frame is derived from a regular hexagon by rotating each edge around the vertex with an offset angle. The side length of the hexagon l and the offset angle α are the primary parameters defining the star-shaped frame. Furthermore, Fig. 1d illustrates other parameters of the unit cell. It indicates that the supporting rods are primarily affected by the interlayer spacing h and the tilt angle θ. It should be pointed out that, θ actually depends on l, h, and α. The relationship between these parameters is given as:

$$\theta = \arctan\left(\frac{h}{\tan\alpha \cdot l}\right) \tag{1}$$

Besides, the diameters of the frame and the supporting rod are referred as d. Hence, the proposed 3D-SAU structure exhibits an excellent tunability of the mechanical properties by adjusting the aforementioned parameters.

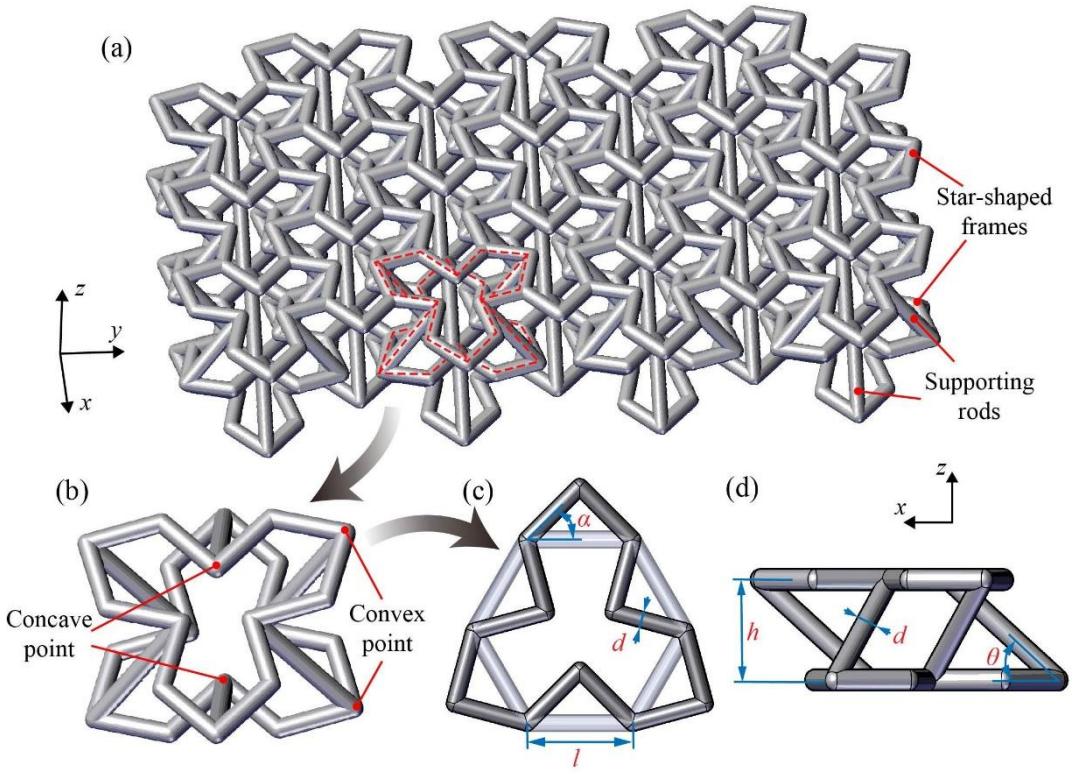

Figure 1: Schematic illustrations of the proposed 3D-SAU structure: (a) the lattice structure, (b) the unit cell, as well as the structural parameter definition of (c) the star-shaped frame and (d) the supporting rod.

2.2 3D-RE and BCC lattice structures

In this study, two types of lattice structures: a 3D-RE[10] and a conventional BCC[11] structure, are employed as reference for comparison, as shown in Fig. 2. For each lattice structure, several structural parameters are selected to define the unit cell. Figs. 2a and b illustrate the lattice structure and unit cell of the 3D-RE structure. The structural parameters of the 3D-RE unit cell include the cell length l_{re}, width w_{re}, height h_{re}, and rod diameter d_{re}, as well as the re-entrant angles θ_{re}. Similarly, Figs. 2c and d present the lattice structure and unit cell of the BCC structure. Additionally, the BCC unit cell is defined using two parameters, the rod diameter d_{bcc} and length l_{bcc}.

3 Study methods

3.1 Parameters of lattice structures

This study compares the mechanical behavior of these three lattice structures via quasi-static compression and LVI tests. Table 1 lists the structural parameters and relative density of these quasi-static compressive specimens. 6×4×2 unit cells are included in each compressive specimen having 3D-SAU structure. To ensure the same relative material density, the 3D-RE and BBC specimens are composed of 11×9×2 and 9×9×2 unit cells, respectively. The relative density is approximately 0.16, and the corresponding compressive specimens as shown in Fig. 3a.

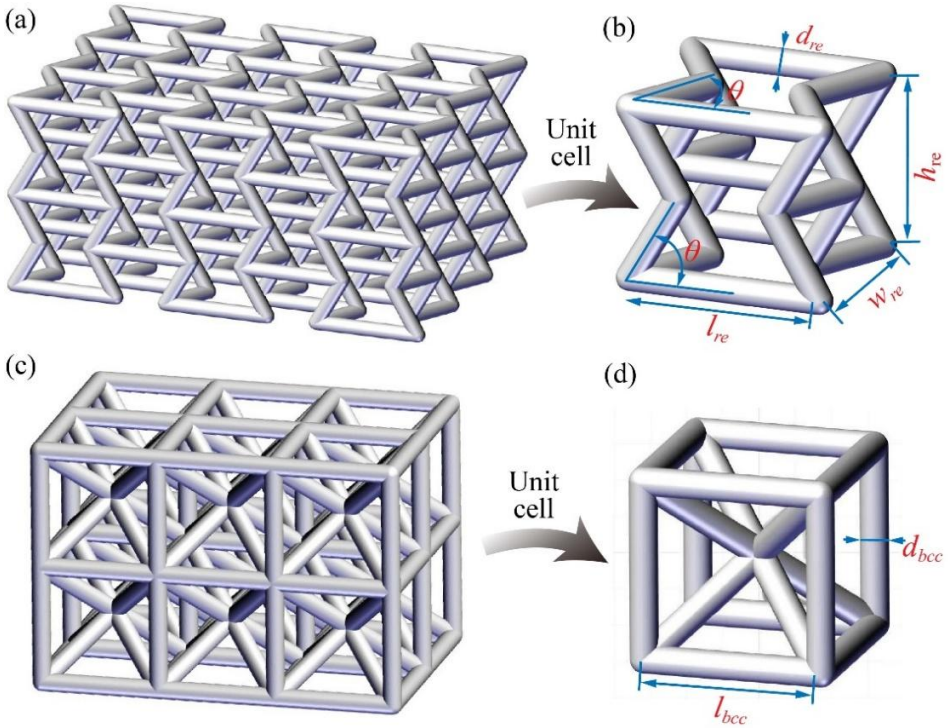

Figure 2 : Schematic illustration of (a,b) the 3D-RE lattice structure and unit cell, as well as (c,d) the BCC lattice structure and unit cell.

Specimen group	Structural parameter	Relative density
3D-SAU-C	l=5.5, h=4.85, α= 45°, d=1.3	0.160
3D-RE-C	l_{re}=5.75, w_{re}=5.1, h_{re}=5.08, θ_{re} = 60°, d_{re}=0.84	0.160
BCC-C	l_{bcc}=5.1, d_{bcc} =0.8	0.160

Table 1: Structural parameters and relative density of the quasi-static compressive specimens. (Unit: mm)

Additionally, the used parameters and corresponding relative density of LVI specimens are listed in Table 2. Notably, these parameters slightly differ from those of the compressive specimens to guarantee same relative density. 15×11×2 3D-SAU, 30×23×2 3D-RE and 29×19×2 BBC unit cells are used to manufacture the lattice cores of these LVI specimens, respectively. In addition, aluminum (Al) cover sheets (Al6061-T6) are employed to fabricate the sandwich structures, as shown in Fig. 3b. The dimension of these cover sheets are 150 × 100 × 1mm^3, and they are bonded to both sides of the lattice cores using epoxy adhesive (ARALDITE 2015-1 C1).

Specimen group	Structural parameter	Relative density
3D-SAU-I	l=5.5, h=4.85, α= 45°, d=1.3,	0.157
3D-RE-I	l_{re}=5.75, w_{re}=5.1, h_{re}=5.1, θ_{re} = 60°, d_{re}=0.8	0.157
BCC-I	l_{bcc}=5.11, d_{bcc} =0.78	0.157

Table 2: Structural parameters and relative density of the LVI specimens. (Unit: mm)

All these lattice structures are fabricated by a 3D printer SPS600B (produced by Shaanxi Hengtong Intelligent Machine Co., Ltd., China) using the Stereo Lithography Appearance (SLA) technique. The photosensitive resin C-UV 9400A (provided by Dongguan Aide Polymer Material Technology Co., Ltd., China) is used for the structure. The additively-manufactured specimens are first placed in an ethanol bath to remove the uncured resin, and then are exposed to UV light for 30 min to guarantee their stable mechanical performance. The density of the post-cured resin is 1.15 g/cm3 , and its Young's modulus and Poisson's ratio are 2649 MPa and 0.4, respectively

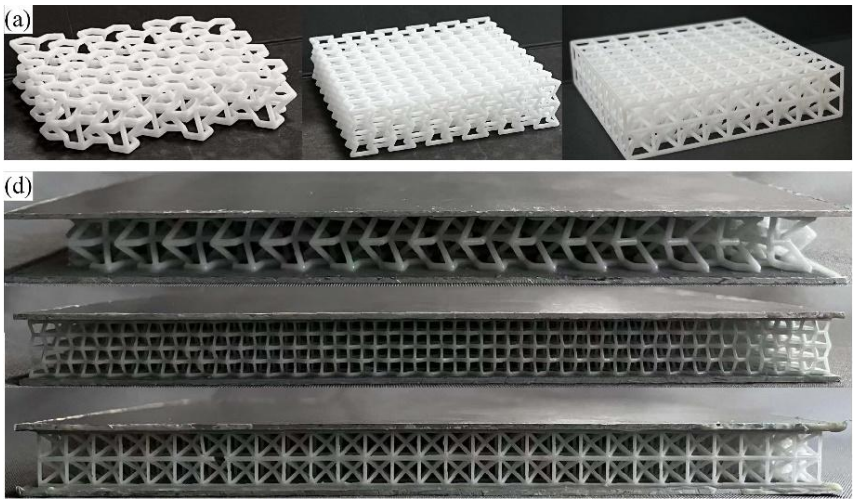

Figure 3 : Lattice specimens used for: (a) quasi-static compressive and (b) LVI tests.

3.2 Experimental study

According to the ASTM C365/C365M-16 standard, quasi-static compressive tests have been carried out by a platform established using a universal testing machine WDW-20C, as demonstrated in Fig. 4a. During the compression process, the specimen is freely placed on the base support, and the compressive displacement is prescribed to the loading plate with a rate of 0.5 mm/min at room temperature. The force and displacement data are directly extracted from the testing machine. Meanwhile, the compression process is recorded using a high-speed camera, I-speed 221, to obtain a detailed observation of the compressive responses.

To assess the LVI responses of these lattice specimens, a testing platform is established according to ASTM D7136/D7136M-20 standard, as illustrated in Fig. 4b. The testing platform employs a WLJ 300 drop-weight impact machine, including a hemispherical impactor, an anti-secondary impact device, a specimen fixture and a

data acquisition equipment. The hemispherical impactor possesses a radius of 12.5 mm and a mass of 2.5 kg, and the anti-secondary impact device is used to prevent the impactor rebound. During the LVI tests, the impact energy is controlled by adjusting the drop height of the impactor. Once the impact energy is determined, the impactor is released from the certain height with no initial velocity, hitting the specimen's center. In this study, two impact energies of 5J and 10J are selected to perform the LVI tests. In addition, a dynamic force sensor (ICP208C05) is utilized to record the transient impact force, and the force-time (F-T) curve is subsequently obtained.

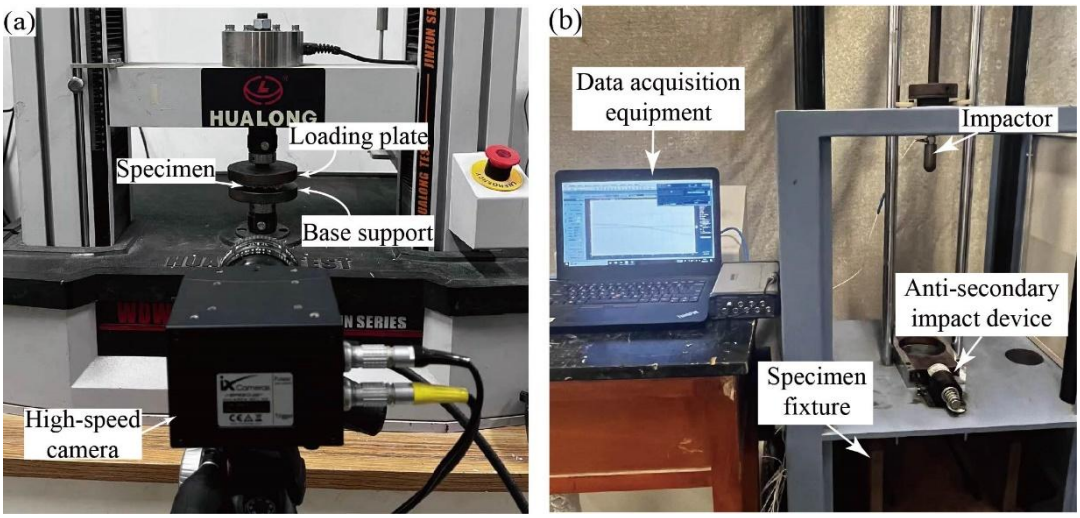

Figure 4 : Experimental testing platform for: (a) quasi-static compressive and (b) LVI tests.

3.3 Simulation study

In this study, an elastoplastic constitutive model is employed in the numerical simulations to capture the mechanical responses of the post-cured photosensitive resin. The elastic parameters are obtained from the supplier and given in Section 3.1, and the plastic parameters are identified from our previous study[12]. Moreover, an isotropic hardening law incorporating the equivalent plastic strain $\varepsilon_{r,eq}$ has been employed to characterize the nonlinear behavior

$$\sigma_{r,eq} = \sigma_{r,0} + Q_1 \cdot (1 - e^{-b_1 \varepsilon_{r,eq}}) + Q_2 \cdot (1 - e^{-b_2 \varepsilon_{r,eq}}) + Q_3 \cdot (1 - e^{-b3 \varepsilon_{r,eq}}) \quad (2)$$

where $\sigma_{r,eq}$ is the equivalent stress, $\sigma_{r,0}$ is the initial yield strength. The parameters Q_i and b_i (i=1,2,3) are the strain hardening parameters and rates, respectively. The first two terms represent the classic Voce hardening law. The third term serves as an additional softening law to govern the Piobert–Lüders behavior, and the fourth term smooths the curve to facilitate the convergence during numerical simulation. Notably, Q_1 and Q_2 are positive and negative values in this equation, respectively. The mechanical parameters in Eq. (2) are obtained from uniaxial tensile tests, and the used parameters are listed in Table 3. Furthermore, a shear damage criterion has been adopted to characterize the damage behavior of the photosensitive resin:

$$D^S = \int \frac{d\varepsilon_{r,eq}}{\varepsilon_{r,eq}^S\left(\theta^S, \dot{\varepsilon}_{r,eq}\right)} \tag{3}$$

where D^S is a state variable, and damage initiation occurs when its value comes to 1. Additionally, $\varepsilon_{r,eq}^S$ is the equivalent plastic strain at the damage onset. The parameter $\varepsilon_{r,eq}^S$ is determined by a function related to the shear stress ratio θ^S and the equivalent plastic strain rate $\dot{\varepsilon}_{r,eq}$. In this study, θ^S and $\dot{\varepsilon}_{r,eq}$ are set to 0.3 and 0.5 s^{-1}, respectively.

Parameter	σ_0 **(MPa)**	Q_1 **(MPa)**	Q_2 **(MPa)**	Q_3 **(MPa)**	b_1	b_2	b_3
Value	28.6	26.2	-22.1	0.8	209.8	55.3	164.2

Table 3: Mechanical parameters of the post-cured photosensitive resin.

The material properties of the Al alloy are obtained from the supplier, with the Young's modulus of 69 GPa and the Poisson's ratio of 0.33. Additionally, the plastic behavior for the Al alloy under dynamic impact load has been captured by the Johnson-Cook constitutive model:

$$\sigma_{Al,eq} = \left(A + B\varepsilon_{Al,eq}^n\right)\left(1 + C\ln\frac{\dot{\varepsilon}_{Al,eq}}{\dot{\varepsilon}_{Al,0}}\right)\left(1 - \left(\frac{T - T_r}{T_m - T_r}\right)^m\right) \tag{4}$$

where $\sigma_{Al,eq}$ is the equivalent stress, $\dot{\varepsilon}_{Al,eq}$ and $\dot{\varepsilon}_{Al,0}$ represent the equivalent plastic and reference strain rates. The parameters A, B, C, m and n represent the initial yield stress, strain hardening modulus, strain rate dependency coefficient, thermal softening exponent and strain hardening exponent, respectively. Additionally, the parameters T, T_r and T_m represent the deformation temperature, the reference temperature and the melting temperature, respectively. The detailed parameters adopted for the Al alloy are listed in Table 4

Parameter	A **(MPa)**	B **(MPa)**	C	m	n	$\dot{\varepsilon}_{Al,eq}$ **(s^{-1})**	T_r **(K)**	T_m **(K)**
Value	159.8	198.39	0.008	1.26	1.31	50	293	855

Table 4: Mechanical parameters of the Al 6061-T6 alloy.

The finite element (FE) model is established according to the actual experimental setup, and the quasi-static compressive and LVI models are illustrated in Fig. 5a and b, respectively. In the quasi-static compressive simulations, the moving plate and base support are considered as rigid bodies, while the specimen is modeled as a solid deformable part. During the compressive modeling, the specimen is positioned between the moving plate and the base support. Meanwhile, the base support is fixed, and a displacement of 7.5mm in z-direction is applied to the moving plate. Additionally, the friction coefficient between the specimen and two plates is set as 0.3, and the friction coefficient within the specimen itself is set as 0.25. The specimen is meshed with tetrahedral elements (element type: C3D10M in Abaqus). After a mesh convergence study, the element dimension of 0.3 mm is selected to ensure both computational accuracy and efficiency. Besides, the rigid bodies are meshed with quadrilateral elements (element type: R3D4 in Abaqus).

In the LVI simulation model, model is established according to the actual experimental setup, as shown in Fig. 5b. In this model, the impactor and fixtures are considered as rigid bodies. During the simulation, the sandwich structure is positioned between two completely fixed fixtures. Additionally, the impactor is assigned a mass of 2.5 kg and is given a velocity along z-direction, with the impact energy controlled by adjusting the impactor velocity. The connection between the lattice core and the cover sheets is assumed as the perfect bonding, and the 'Tie' constraint is correspondingly employed. Furthermore, a general contact with a friction coefficient of 0.3 is applied in this model. To improve the computational efficiency, the lattice core is discretized using 2-node linear beam elements (element type: B31 in Abaqus). The other parts are discretized using 8-node linear brick elements (element type: C3D8R in Abaqus). The element size in the impact and non-impact regions is set to 0.3 mm and 1 mm, respectively. The FE mesh ensures both computational accuracy and efficiency.

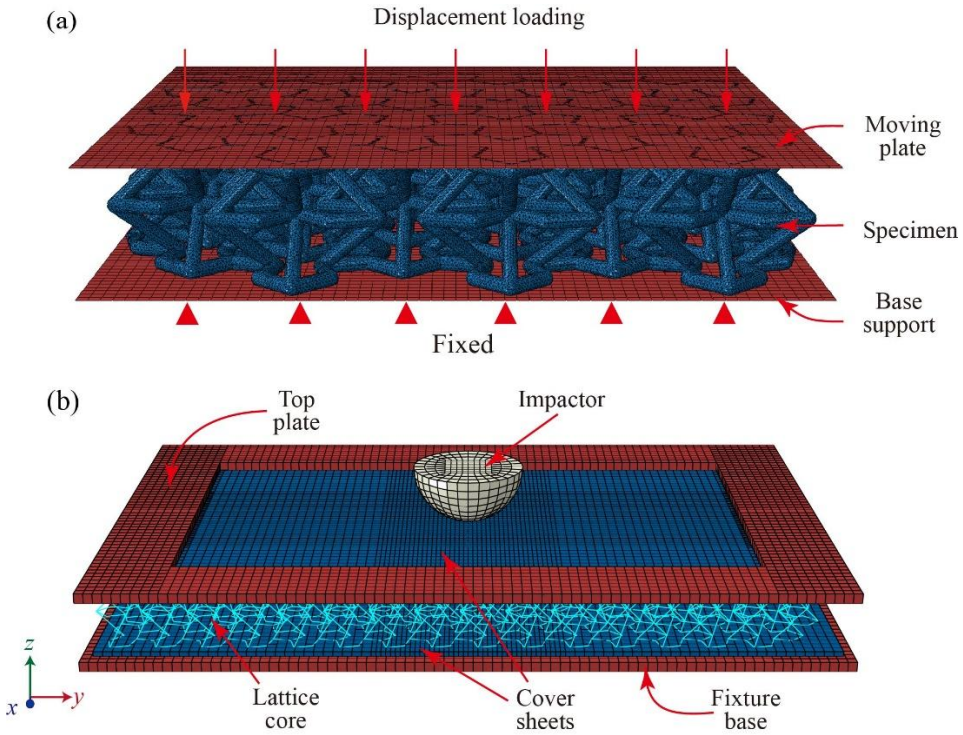

Figure 5 : FE model of the numerical (a) quasi-static compressive and (b) LVI tests.

4 Results and Conclusions

4.1 Validation of numerical modeling

In this section, the numerical results are compared with the experimental ones to validate the accuracy of the numerical models. A group of three tests have been performed to ensure the reproducibility of the experimental results. Fig. 6 depicts the force-displacement (*F-D*) curves extracted from the experimental and numerical compressive tests. It is observed that, the numerical results possess good agreement with the experimental ones. During the compressive tests, all three types of lattice

structures exhibit three distinct stages: the linear stage, the stress plateau stage, and the densification stage (marked as stages A, B and C in Fig. 6).

Within the linear stage, the structural stiffnesses computed from the numerical results align well with the experimental ones. However, as the curves begin to enter the stress plateau stage, the predicted transition points occur earlier than the experimental ones. Table 5 lists the mean plateau forces F_{plat} of these lattice structures, with the corresponding averages and standard deviations derived from three repeated tests for each experimental group. Additionally, the relative errors between the experimental and numerical results are calculated accordingly. The maximum error of these lattice structures is 5.0%. Additionally, in the stress plateau and densification stages, the numerical model accurately captures the transition points of the lattice structures compressive loads. Comprehensively considering the relative errors and curve trends, the numerical model is considered to possess the capacity to accurately capture the compressive responses.

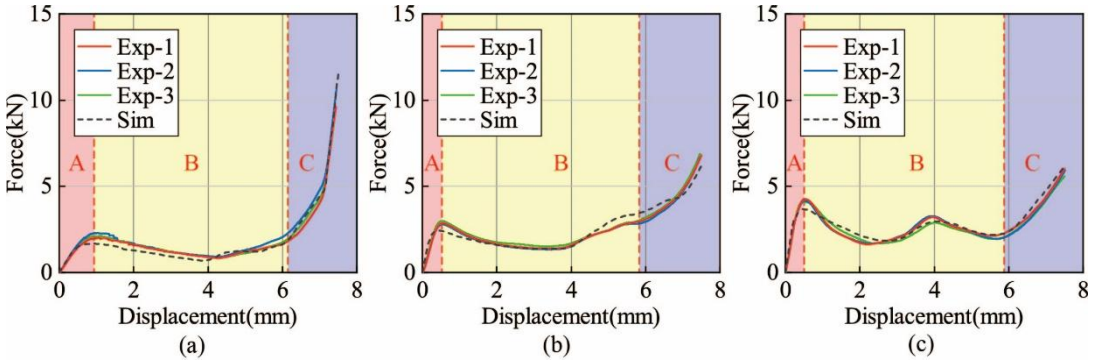

Figure 6: Comparisons of the *F-D* curves obtained from the experimental and numerical quasi-static compressive tests of: (a) the 3D-SAU, (b) 3D-RE and (c) BCC lattice structures.

Specimen group	Exp-1	Exp-2	Exp-3	Avg	SD	Sim	Error
3D-SAU-C	1.35	1.48	1.39	1.41	0.05	1.34	5.0%
3D-RE-C	2.03	2.04	2.21	2.06	0.04	2.16	4.7%
BCC-C	2.46	2.44	2.40	2.43	0.02	2.51	3.2%

Table 5: Average relative errors of the mean plateau forces F_{plat} between the experimental and numerical quasi-static compressive tests. (Unit of F_{plat}: kN)

In the dynamic LVI simulations, the velocities of the impactor at the onset of impact are set at 2 m/s and 2.83 m/s, corresponding to impact energies of 5J and 10J, respectively. Fig. 7 depicts the force-time (*F-T*) curves extracted from the experimental and numerical LVI tests. During the LVI tests, the sandwich structures exhibit two stages: the impact stage and the rebound stage (marked as stages A and B in Fig. 7).

In the impact stage, all the numerical results show good agreement with the experimental ones. However, in the rebound stage, there exists a discrepancy between

the experimental and numerical results of BCC sandwich structure. The discrepancy is primarily caused by the beam-element model which possess the limitation in accurately capturing the buckling behavior of rod. Whereas the BCC lattice structure contains vertically-oriented rods that experience buckling during LVI test. Additionally, Table 6 lists the peak force F_{peak} obtained from experimental and numerical results, and the experimental averages, standard deviations, as well as the relative errors are calculated accordingly. The maximum error is 11.4%, occurring in the BCC sandwich structure under LVI of 5J impact energy. For the 3D-SAU and 3D-RE sandwich structures, the errors are less than 2.1%. These results reveal that, the numerical models possess the capacity to predict the impact behaviors of the sandwich structures.

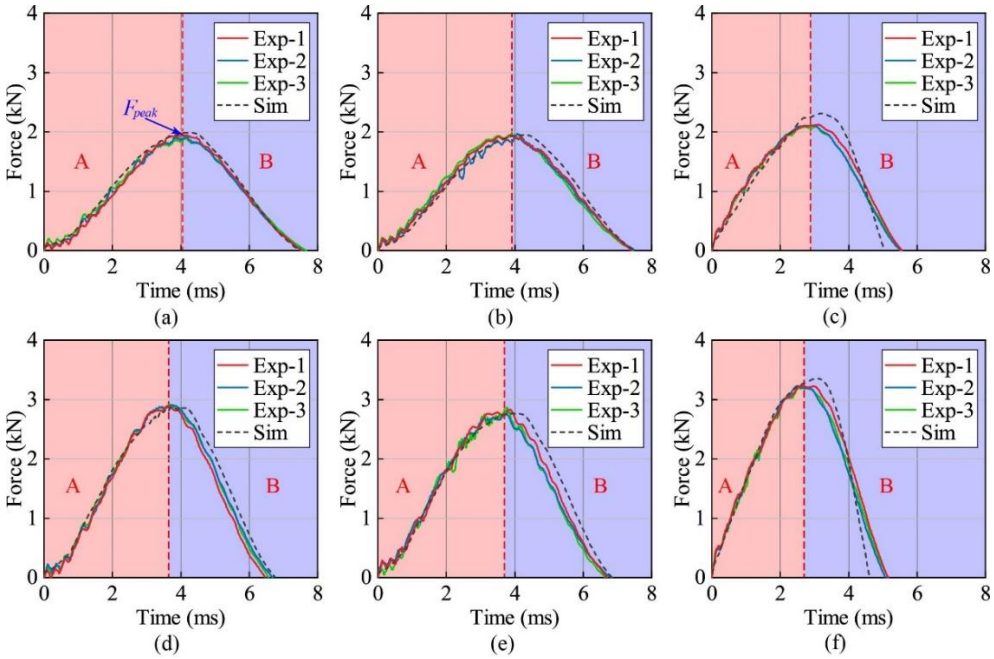

Figure 7: Comparisons of the *F-T* curves obtained from the experimental and numerical dynamic LVI tests of: (a-c) 5J impact energy and (d-f) 10J impact energy. (a,d), (b,e) and (c,f) refer to specimen groups 3D-SAU-I, 3D-RE-I and BCC-I, respectively

Specimen group	Exp-1	Exp-2	Exp-3	Avg	SD	Sim	Error
3D-SAU-I-5J	1.89	1.92	1.95	1.92	0.02	1.96	2.1%
3D-RE-I-5J	1.94	1.96	1.96	1.95	0.01	1.97	0.9%
BCC-I-5J	2.12	2.10	2.11	2.11	0.01	2.35	11.4%
3D-SAU-I-10J	2.92	2.91	2.89	2.91	0.01	2.86	1.7%
3D-RE-I-10J	2.83	2.77	2.87	2.82	0.04	2.76	2.1%
BCC-I-10J	3.23	3.21	3.23	3.22	0.01	3.34	3.7%

Table 6: Average relative errors of the peak forces F_{peak} between the experimental and numerical LVI tests. (Unit of F_{peak}: kN)

4.2 Mechanical behavior of 3D-SAU and other lattice structures

In this section, the mechanical behavior of the proposed 3D-SAU lattice structure is compared with the 3D-RE and BCC structures. Since the experimental results exhibit a relatively high consistency, the median one has been selected as the representative of each testing group for the comparison.

Fig. 8 illustrates the stress-strain curves obtained for three types of lattice structures under quasi-static compressive loads. It can be observed that the 3D-SAU lattice structure possesses a longer linear stage than other two structures. While, the durations of the linear stage for the 3D-RE and BCC lattice structures are almost similar. The computed stiffnesses of the 3D-SAU, 3D-RE, and BCC structures from stress-strain curve are 10.78 MPa, 14.66 MPa, and 54.39 MPa, respectively. In the compression process, the stress plateau stage is frequently considered as a crucial stage for sandwich core structure, since a stable and prolonged stress plateau significantly enhances the energy-absorption capacity. Among these three structures, the stress plateau of BCC exhibits unstable stresses with slightly increasing trend with increasing displacement. This rise is caused by the self-contact occurring within the BCC lattice structure during compression. Moreover, both the 3D-SAU and 3D-RE lattice structures possess a stable stress plateau stages. And, the 3D-SAU one exhibits a relatively lower and more stable plateau stress. These observations reveal that, the 3D-SAU structure is capable of absorbing more deformation energy without rising the stress level, thereby providing more effective protection for internal components.

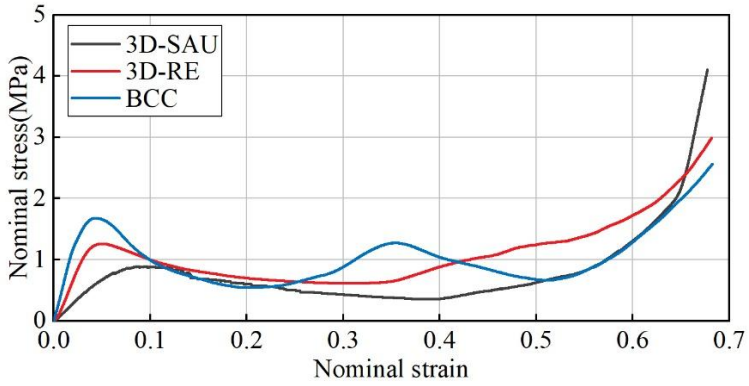

Figure 8: Experimental stress-strain curves obtained for 3D-SAU, 3D-RE and BCC lattice structures under quasi-static compression.

The LVI responses of different sandwich structures are compared in Fig. 9. Thereinto, the *F-D* curves are computed from the *F-T* curves. As shown in Fig. 9a, the BCC structure possesses the highest peak force and the shortest impact duration. In comparison, the two types of auxetic structures exhibit similar LVI responses with lower peak forces and longer impact durations in each impact energy case. These features suggest that the auxetic structures provide the superior protective performance during LVI process. Additionally, the 3D-SAU structure exhibits slightly larger impact displacement compared with the 3D-RE structure. This larger displacement enables the 3D-SAU structure to dissipate more impact energy, potentially improving the protective effectiveness.

To further investigate the impact behaviors of these lattice structures, the energy-absorption efficiency (η) and the specific energy-absorption (SEA) are illustrated in Fig. 10. It can be observed that, the BCC structure exhibits a slightly higher energy-absorption capacity in the low impact energy case (5J). However, in the high impact energy case (10J), the two types of auxetic structures reveal the better energy-absorption capacity. In addition, the energy-absorption efficiency of the 3D-SAU and 3D-RE structures shows significant improvement, as the impact energy increases. It is attributed to these structures exhibiting an enhanced auxetic effect in the high impact energy case.

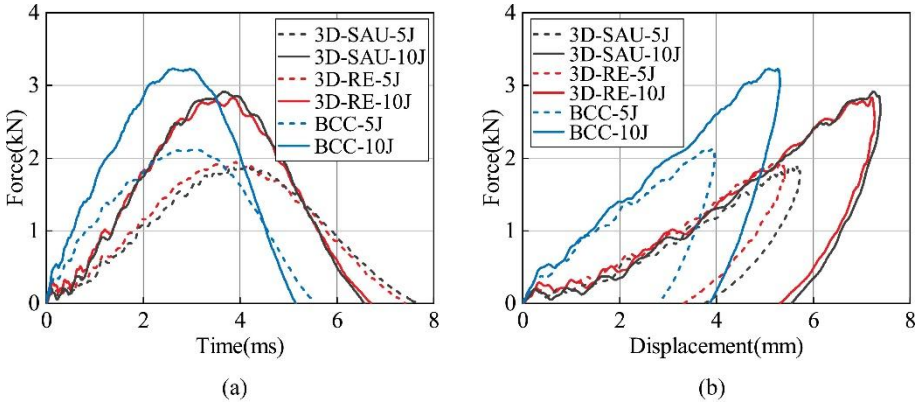

Figure 9: Experimental mechanical responses obtained for 3D-SAU, 3D-RE and BCC lattice structures under dynamic LVI: (a) *F-T* and (b) *F-D* curves.

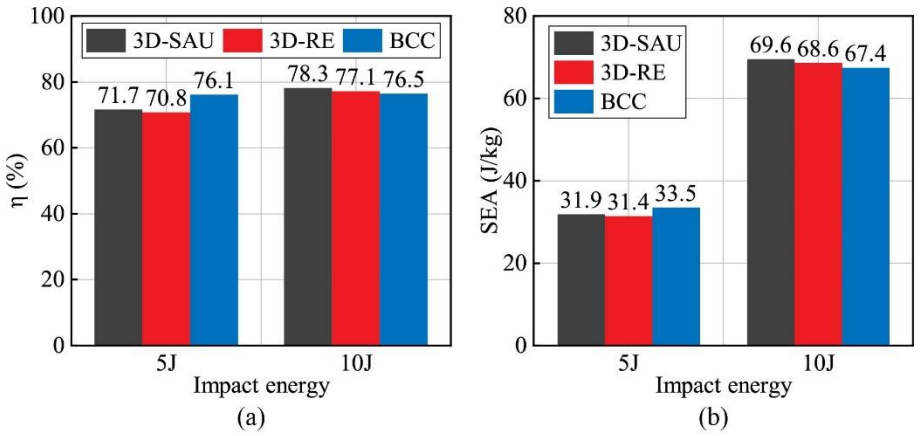

Figure 10: (a) Energy-absorption efficiency (η) and (b) specific energy-absorption of 3D-SAU, 3D-RE and BBC lattice structures subjected to LVIs with 5J and 10J impact energies.

Moreover, the LVI damages of these specimens are primarily characterized by visible dents on the top cover sheet. Subsequently, the impact dent areas on the top cover sheets of these lattice structures are measured using an optical microscope (OM) Keyence® VHX-6000. Table 7 lists the measured dent areas, with the average values and standard deviations calculated accordingly. It can be observed that, the BCC structure possesses the largest dent area. In the low impact energy case (5J), the dent areas have been reduced to 36.5% and 30.8% for the 3D-SAU and 3D-RE structure compared to the BCC one. In the high impact energy case (10J), the reduction are

32.1% and 26.5%, respectively. This reduction is mainly attributed to the auxetic behavior under impact loads. When subjected to impacts, these auxetic structures gather towards the impacted region, where the material density is increased accordingly. The increasing of material density is capable of enhancing the local impact-resistance, inhibiting the growth of the impact dent. In addition, the dent area of the 3D-SAU structure is slightly smaller than that of the 3D-RE one. It indicates that, the 3D-SAU structure possesses the better auxetic effect under impact loads, offering the superior impact-resistance than the other two structures

Specimen group	Exp-1	Exp-2	Exp-3	Avg	SD
3D-SAU-I-5 J	26.79	24.49	28.73	26.67	1.73
3D-RE-I-5 J	28.29	30.42	28.52	29.08	0.95
BCC-I-5 J	38.60	44.56	42.58	42.00	2.51
3D-SAU-I-10 J	50.90	51.50	49.83	50.74	0.69
3D-RE-I-10 J	55.85	55.61	53.26	54.91	1.17
BCC-I-10 J	70.26	76.56	77.37	74.73	3.18

Table 6: Impact dent areas on the top cover sheets of the lattice structures obtained by optical microscope. (Units of area: mm^2)

4.3 Conclusions

This paper proposes a novel 3D star-shaped auxetic (3D-SAU) structure and compare it with classical body-centered-cubic (BCC) and 3D re-entrant (3D-RE) ones. The mechanical properties have been experimentally and numerically investigated through quasi-static compressive and LVI tests. Within the quasi-static compressive simulation, the lattice structure is discretized using solid elements to accurately capture the densification stage. While, beam elements are employed to discretize the lattice structure, aiming to guarantee the computational accuracy and efficiency. The following conclusions can be drawn from the paper:

1. The numerical results align well with experimental ones. Both quasi-static compressive and dynamic LVI simulations successfully capture the mechanical and damage behaviors, with maximum errors of 5.0% and 11.4% for F_{plat} and F_{peak}, respectively. It reveals the accuracy and reliability of these modeling approaches for the lattice structures.

2. During the compressive tests, the 3D-SAU structure exhibits a prolonged and lowest stress plateau stage compared to the two others with the same relative density. Additionally, the 3D-SAU structure absorbs more energy during the linear stage. This suggests that the 3D-SAU structure is capable of providing effective protection for internal components.

3. During LVI tests, the auxetic structures (3D-SAU and 3D-RE) exhibit lower peak forces, longer impact durations, and higher energy absorption efficiency under high

impact energy (10J). Additionally, the 3D-SAU structure demonstrates the smallest impact dent. These results confirm the superior energy-absorption and impact-resistance performance of the 3D-SAU structure.

Acknowledgements

The authors acknowledge the financial supports from National Natural Science Foundation of China (No. 52005451 and 52305292). This study is also supported by Joint Fund of Research and Development Program of Henan Province (No. 222301420033).

References

[1] Y. Li, W. Qiu, Z. Liu, Y. Liu, L. Xia, A multi-material topology optimization approach to hybrid material structures with gradient lattices, Computer Methods in Applied Mechanics and Engineering 425 (2024) 116969.

[2] J. Li, Q. Qin, J. Zhang, Internal blast resistance of sandwich cylinder with lattice cores, International Journal of Mechanical Sciences 191 (2021) 106107.

[3] J. Shen, S. Zhou, X. Huang, D. Ruan, Y. M. Xie, J. Shen, S. Zhou, X. Huang, D. Ruan, Y. Xie, Inertia effect on buckling-induced auxetic metamaterials, International Journal of Protective Structures 6 (2015) 311–322.

[4] H. Guo, H. Yuan, J. Zhang, D. Ruan, Review of sandwich structures under impact loadings: Experimental, numerical and theoretical analysis, Thin-Walled Structures 196 (2023) 111541.

[5] C. Wang, Y. Li, W. Zhao, S. Zou, G. Zhou, Y. Wang, Structure design and multi-objective optimization of a novel crash box based on biomimetic structure, International Journal of Mechanical Sciences 138-139 (2018) 489–501.

[6] L. Foster, P. Peketi, T. Allen, T. Senior, O. Duncan, A. Alderson, Application of auxetic foam in sports helmets, Applied Sciences 8 (3) (2018) 354.

[7] H. Lu, X. Wang, T. Chen, The quasi-static responses and variable mechanical properties of a novel 3D composite auxetic tubular structure connected by the thin-walled tube, Composite Structures 324 (2023) 117573.

[8] X. Ren, J. Shen, P. Tran, T. D. Ngo, Y. M. Xie, Design and characterisation of a tuneable 3D buckling-induced auxetic metamaterial, Materials & Design 139 (2018) 336–342.

[9] C. Li, H.-S. Shen, J. Yang, Multi-scale modeling and numerical analysis of sandwich beams with FG auxetic 3D lattice cores and GRC face sheets subjected to drop-weight impacts, Engineering Structures 265 (2022) 114486.

[10] Y. Xue, X. Wang, W. Wang, X. Zhong, F. Han, Compressive property of Al-based auxetic lattice structures fabricated by 3D printing combined with investment casting, Materials Science and Engineering: A 722 (2018) 255–262.

[11] Q. He, Y. Hou, X. Li, S. Li, L. Meng, Investigation on the compressive behavior of hybrid polyurethane (PU)-foam-filled hyperbolic chiral lattice metamaterial, Polymers 15 (9) (2023) 2030.

[12] S. Li, Y. Hou, J. Huang, J. Shi, L. Meng, Exploring the enhanced energy-absorption performance of hybrid polyurethane (PU)-foam-filled lattice metamaterials, International Journal of Impact Engineering 193 (2024) 105058.